

Effect of enhanced cooling on microstructure evolution of alloy 718 using the gas tungsten arc welding process

SGK. Manikandan¹ · D. Sivakumar¹ · K. Prasad Rao² · M. Kamaraj³

Received: 19 July 2015 / Accepted: 20 April 2016 / Published online: 29 April 2016
© International Institute of Welding 2016

Abstract The microsegregation in alloy 718 fusion zone during gas tungsten arc welding affected the aging response and the mechanical properties. The average weld cooling rate was enhanced in gas tungsten arc (GTA) welding process by employing liquid nitrogen during the process. The combination of in-process and external cooling methods reduced the microsegregation of Nb in alloy 718 fusion zone. Detailed characterization of the weld microstructures in the as-welded and the direct aged conditions was conducted. The dendritic structure have been refined to a level of 10–20 μm dendrite arm spacing and Laves particle sizes ranging from 0.04 to 1.43 μm due to the enhanced weld cooling rate. Similarly, the average Laves volume fraction was reduced from 45 to 0.1 % when compared to the conventionally cooled GTA welding process. The microsegregation was quantified through the computed solidification time through the DSC analysis and the volume fraction of the eutectic phases. It was found that the solidification time was reduced significantly from 2.499 s to as low as 0.36 s with the liquid nitrogen-

cooled GTA welding process. The microhardness survey revealed an improved aging response of the fusion zone.

Keywords (IIW Thesaurus) GTA welding · Nickel alloy · Cooling rate · Segregation · Pulsed arc welding

Abbreviations

CCAR	Constant current argon
CCPAR	Compound current argon
CCHE	Constant current helium
CCPHE	Compound current helium
EBW	Electron beam welding
AW	As welded
DA	Direct aged
STR	Solidification temperature range
t_s	Solidification time
DTA	Differential thermal analysis
DSC	Differential scanning calorimetry
GTAW	Gas tungsten arc welding
Act	Actual
Nom	Nominal

Highlights

- Interdendritic segregation has been controlled
- Laves phase formation have been studied with liquid nitrogen cooling
- Microfissure-free HAZ is demonstrated at higher cooling rates with LN_2 cooling
- Aging response with solid solution filler metal have been demonstrated

Recommended for publication by Commission IX - Behaviour of Metals Subjected to Welding

✉ SGK. Manikandan
nehakutty06@gmail.com

¹ Indian Space Research Organization, Trivandrum, India

² University of Utah, Salt Lake City, UT, USA

³ Indian Institute of Technology Madras, Chennai, India

1 Introduction

The nonequilibrium solidification resulted in the formation of chemical inhomogeneity and the consequent interdendritic Laves phase during welding of alloy 718 [1]. Hence, faster cooling rate was employed using pulse current welding process which reduced the level of interdendritic Nb segregation and the amount of Laves phase [2–5]. A study on the combined effect of helium shielding gas and the modified pulse waveform on alloy 718 fusion zone revealed that the Laves phase was reduced because of the enhanced weld cooling rate

and the steeper temperature gradient [5–7]. Use of electron beam welding (EBW) with beam oscillations enhanced the weld cooling rate due to lower-energy input rate [8]. The beneficial effects of the EBW process could not be utilized in the rocket engine welded joints because of the complex structure and restricted accessibility to the weld joints. Hence, a study on the rapid heat dissipation using liquid nitrogen was initiated with manual gas tungsten arc (GTA) welding process for enhancing the weld cooling rate.

The maximum temperature and the time at temperature during welding were the controlling factors for the microsegregation. The microsegregation was reduced by shortening the time at temperature during welding. Different methodologies were reported for studying the time-temperature effects. In the present work, heat generated during welding was dissipated by the liquid nitrogen-cooled copper base plate which was in contact with the weldment. Similar works were reported for the grain refinement in ferritic stainless steel welds [9] and the distortion control in laser welding with solid CO₂ [10]. In the present study, liquid nitrogen cooling was employed during welding and resultant microstructures were analyzed.

2 Experimental setup

2.1 Materials

Alloy 718 sheets (2 mm thick) in solution-treated condition were joined by gas tungsten arc welding (GTAW) process using a filler metal of size Φ 1.6 mm. Two types of filler metals such as solid solution filler metal (FM1, near equivalent to ERNiCrMo-7) and age-hardenable filler metal (FM2, ERNiFeCr-2) were used. The details of the chemical composition of base material and filler metal are given in Table 1. The solid solution filler metal (FM1) had reduced Fe and Cr contents (Laves stabilizers), and also, it did not contain Nb. Hence, the reported Nb content of FM1 fusion zone in the present work was the result of weld dilution from the base material.

2.2 Welding procedure

Square butt joints with tight fit-up were used. An optimized heat input value of 0.75 to 0.77 kJ/mm was used [6]. The welding fixture consisted of a box-like structure with a copper

cooling system and supporting plates. The weld coupons were rigidly clamped to the welding fixture, in such a way that they were in contact with the copper plate as shown in Fig. 1a, b, c. Two modes of welding current such as constant and compound current pulse (a modified pulse waveform) were employed as shown in Fig. 1d. The pulse waveform was derived using the hybrid pulsing concepts from the previous works [11, 12]. Similarly, argon and helium gases were used as shielding gases. Hence, four combinations of the experiments (CCAR, CCPAR, CCHE, and CCPHE) were carried out.

The cooling system had a hole of 12 mm diameter at the outlet end for avoiding pressure buildup by nitrogen vapor during the welding process. The entire assembly was kept inside the welding hood and sealed. The welding hood was media substituted with helium gas. Thereby, ice formation (from moisture in air) was avoided in the weld coupon and the copper cooling system while in contact with liquid nitrogen. Liquid nitrogen was supplied through the inlet of copper cooling system, and the entire system temperature was stabilized. During welding, the LN₂ became nitrogen vapor by extracting the heat. Thus, a mixed flow (LN₂ and cold nitrogen vapor) could be achieved since the balancing of LN₂ inflow rate and the boiling rate was found to be difficult to control during the welding process.

2.3 Microstructural characterization methods

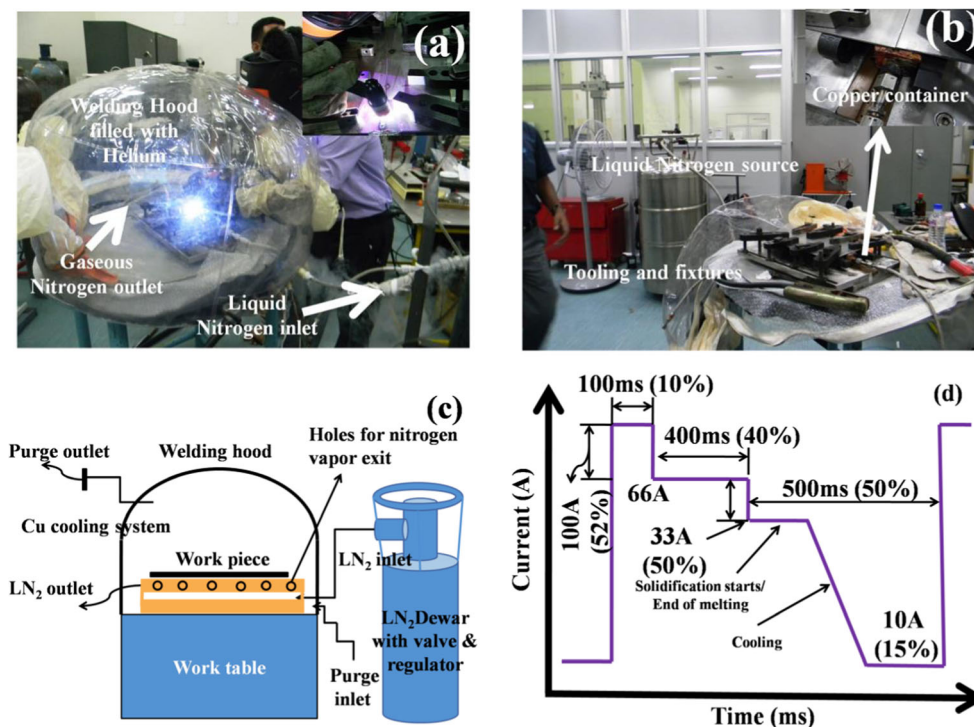
Welded samples were checked for defects by 100 % X-ray radiography and dye penetrant test. The samples were prepared by the standard metallographic technique and etched using Kalling's reagent. Scanning electron microscopy was conducted on weld metal samples using field emission gun scanning electron microscopy (FEG-SEM) with an acceleration voltage of 30 kV and a resolution of 1.2 nm. The weld fusion zone was removed and polished with standard procedure for the phase identification by X-ray diffraction with Cu-K α radiation.

The differential thermal analysis was conducted on the base material, the filler metal (FM1), and the FM2 fusion zone using SII 6300 EXSTAR with a measurement range of \pm 1000 μ V and a sensitivity of 0.06 μ V. Three heating rates (5, 10, and 20 °C/min) and a cooling rate of 50 °C/min were used with a sample weight of 0.02 ± 0.0005 g for the analysis. The entire thermal analysis was carried out in an argon atmosphere with a flow rate of 0.2 l/min. The heating rate was

Table 1 Chemical composition of base metal and filler metals

Elements	C	Mn	Si	Cr	Fe	Mo	Nb + Ta	Ti	Al	Cu	Ni	
Alloy 718	0.05	0.11	0.11	18.15	19.77	2.89	5.02	1	0.62	0.03	Bal	Act
ERNiCrMo-7	0.05	2	0.5	16	5	16	–	–	–	–	Bal	
ERNiFeCr-2	0.08	0.55	0.35	21	16	3.3	5.5	1.15	0.8	0.3	Bal	Nom

Fig. 1 Experimental setup (a, b). Schematic of the experimental setup c with liquid nitrogen cooling and d modified pulse waveform



finalized based on the results of differential thermal analysis (DTA) experiment for differential scanning calorimetric (DSC) analysis. Differential scanning calorimetric analysis was performed on a SETARAM LABSYS 1600 heat flux-type DSC instrument with platinum–rhodium DSC rod using specimens of 0.2 g. The described equipment is capable of handling temperature from ambient to 1600 °C with an isothermal temperature accuracy of ± 1 °C and precision within ± 0.04 °C. The equipment was calibrated with melting points and enthalpy of fusion for In, Sn, Pb, Al, Ag, Au, and Ni elements. Specimens were heated at a rate of 20 °C/min up to 500 °C, and then, heating rate was changed to 10 °C/min till 1500 °C under argon atmosphere. Then, the samples were cooled at 20 °C/min through the solidification temperature range in an inert atmosphere. Reaction temperatures were calculated by determining the temperature at which the DSC curve deviated from the local baseline in heating curve using the first derivative method.

Disks of 3 mm diameter were punched out from the thin foils of 90 μm thickness from the base material and the as-welded fusion zone. These disks were further thinned down by twin-jet electro-polishing technique with an applied voltage of 18 ± 2 V. The electrolyte used was one part of perchloric acid and four parts of ethanol at a temperature of approximately -40 °C. These foil type specimen were observed using JEOL-make transmission electron microscope (TEM) equipment. Elemental composition was obtained across the dendritic and the interdendritic regions in metallographically prepared, unetched specimens with a JEOL JXA-8530F thermal

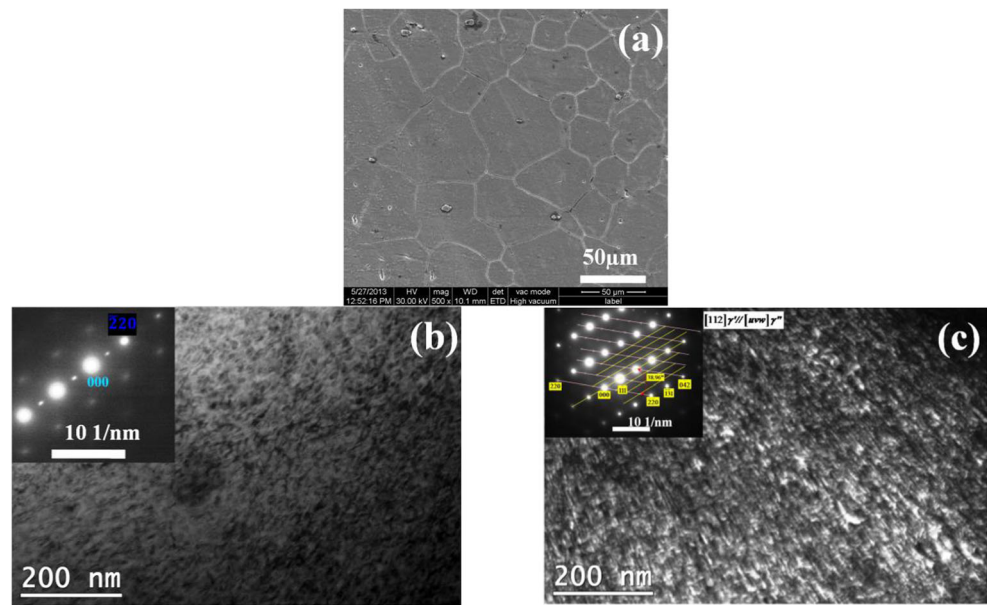
field emission electron microprobe (EPM) using an acceleration voltage of 15 kV and a probe current of 50 nA with a beam diameter of 100 nm. The compositions for the following elements were quantitatively determined: Cr, Fe, Mo, Nb, Ni, Si, Al, and Ti. Welded samples were subjected to two-step aging heat treatment cycle of 720 °C for 8 h and 620 °C for 8 h and then cooled down to room temperature as per standard AMS 5596 K. The age-hardening response of the fusion zone was analyzed by Vickers microhardness measurement. The load applied was 300 gf (2.942 N) for the duration of 15 s in the as-welded specimen and 1000.04 gf (9.807 N) load for 15 s, in the case of the direct aged sample.

3 Results and discussion

3.1 Microstructural characterization of fusion zone

The base material in the as-received condition (980 °C solution-treated condition) consisted of fine equiaxed austenite grains (16.8 μm) of ASTM no. 8.5 as shown in Fig. 2a. The TEM dark field micrographs of the direct aged base material that exhibited γ' and γ'' precipitates are shown in Fig. 2b, c with the crystal structure of L1_2 -ordered FCC and DO_{22} BCT. The liquidus and solidus temperatures of the base material were measured to be 1364 ± 2 and 1319 °C ± 2 °C, respectively. The possibility of secondary phase formation in FM1 filler metal was studied through DTA and found no secondary phases upon cooling. The liquidus and solidus temperatures

Fig. 2 Base material **a** SEM secondary electron image in 980 °C solution-treated condition and TEM images of **b** γ' and **c** γ'' precipitates in direct aged condition



of the FM1 filler metal were 1397 ± 2 and 1375 ± 2 °C, respectively. Because of the slow heating and cooling rates used for DTA, these values represent the equilibrium liquidus and solidus temperatures. The process variables were employed from the earlier work [6]. The weld cooling rates could not be measured due to the limitations in the present test setup. However, the average weld cooling rates were calculated from the measured dendrite arm spacing from FE-SEM micrographs using the correlation developed in our previous work [6]. The average weld cooling rates were enhanced due to the rapid heat extraction from the copper fixture which was in contact with the weld metal by LN₂ cooling. The fusion zone microstructures of conventionally cooled method were presented for comparison with the LN₂-cooled fusion zone.

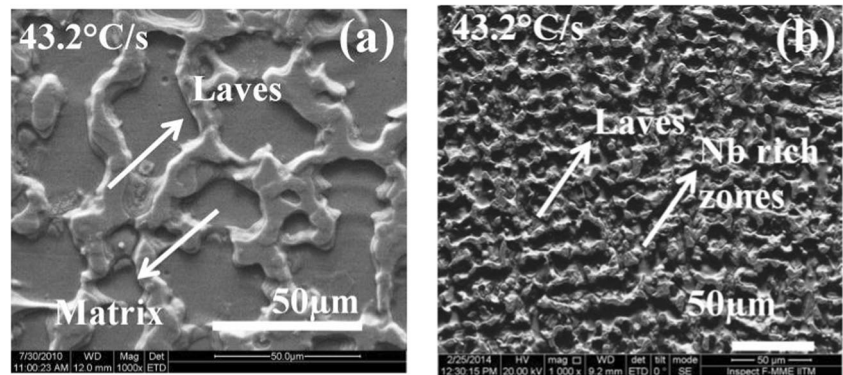
Thick and continuous Laves network was reported for the maximum instantaneous weld cooling rate of 43.2 °C/s in FM1 and FM2 fusion zones [5, 6] as shown in Fig. 3a, b. The weld cooling rates mentioned in the present work were measured over the temperature range of 1100 to 200 °C. The same were extrapolated to 1400 °C, and the cooling rates were calculated from 1400 to 900 °C considering the phase transformation temperatures of the present alloy system. The details of cooling rate measurement were discussed in our previous work [6]. A set of process variables of constant current (50 ± 2 A) and argon gas shielding was employed for achieving the weld cooling rate of 43.2 °C/s. Because of the lower weld cooling rate employed in the present study, the microsegregation in the interdendritic regions was increased and led to the formation of thick and continuous Laves network. The microsegregation and dendrite arm spacing were observed to be different for FM1 and FM2 fusion zones at lower and intermediate weld cooling rates [13]. The Mn content in FM1 filler metal could play a role of deoxidizer during

welding which resulted in the formation of manganese oxides prior to solidification and acted as nuclei. Moreover, the Mn content in FM1 filler metal lowered Si in the matrix and thus Nb-rich phases by prompting oxides. This resulted in the reduction of Nb-rich phases in the interdendritic regions of the fusion zone. In addition to the above, it was reported that increasing the Mn content coarsened the dendrites [14–16].

Upon varying the pulse waveform (compound current pulse with superimposed peak current of 100 ± 2 A, peak current of 66 ± 2 A, and a base current of 33 ± 2 A as shown in Fig. 1d) and the usage of helium gas for shielding, the maximum instantaneous weld cooling rate was enhanced from 43.2 to 394.3 °C/s. Further improvement in the cooling rate was achieved by the liquid nitrogen cooling during welding with the same set of weld parameters employed in the conventional cooling method. The continuous Laves network was eliminated with LN₂ cooling for the same set of process variables (as used for the instantaneous weld cooling rate of 43.2 °C/s) as shown in Fig. 4a. The interdendritic segregation was significantly reduced due to the faster cooling of molten pool with LN₂ chilling which promoted rapid heat dissipation [17]. The FE-SEM/energy dispersive spectroscopy (EDS) analysis of the interdendritic phases in FM1 fusion zone revealed Nb (11.49 wt%), although the filler metal FM1 did not contain Nb. This could be because of the weld dilution from the base material. However, the results of X-ray and electron diffraction studies confirmed the presence of Fe₂Nb, and the same have been discussed.

The combined effect of the unfavorable segregation time for the solute elements with partition coefficient less than one and lower diffusivity and mobility of heavier solute elements (Nb, Mo) and faster cooling rate were aided in reducing the microsegregation. Similar mechanisms were operative in the

Fig. 3 Secondary electron micrographs of conventionally cooled **a** FM1 and **b** FM2 fusion zone



other fusion zones with average weld cooling rates of 361.8 and 297.8 °C/s as shown in Fig. 4c, e. Whereas in the case of fusion zone with an average weld cooling rate of 508.7 °C/s, fine equiaxed dendritic structure was found with finer laves

particles in the interdendritic region as shown in Fig. 4g. This could be due to the combined effect of reduced time at temperature and local solidification time, enhanced weld cooling rate and resultant undercooling, lower mobility and diffusivity of larger solute elements (Nb, Mo), and the existence of steep temperature gradients. Moreover, the equiaxed dendrite side arm was growing in the direction of imposed temperature gradient as in Fig. 4g. Similar observations were made in the fusion zones of FM2 for the same set of process variables (264.9, 297.8, 361.8, and 508.7 °C/s) as that of the FM1 fusion zone as shown in Fig. 4b, d, e, h. The dendrite arm spacing of LN₂-cooled FM1 and FM2 fusion zones were finer when compared to the conventionally cooled fusion zones. The dendrite coarsening phenomenon observed in the conventionally cooled fusion zone of FM1 filler metal was not effective over the dendrite arm spacing in the LN₂-cooled fusion zones. This could be probably due to the enhanced weld cooling rates. Similar observations were made in the higher cooling rate (394.3 °C/s) conventionally cooled process [13].

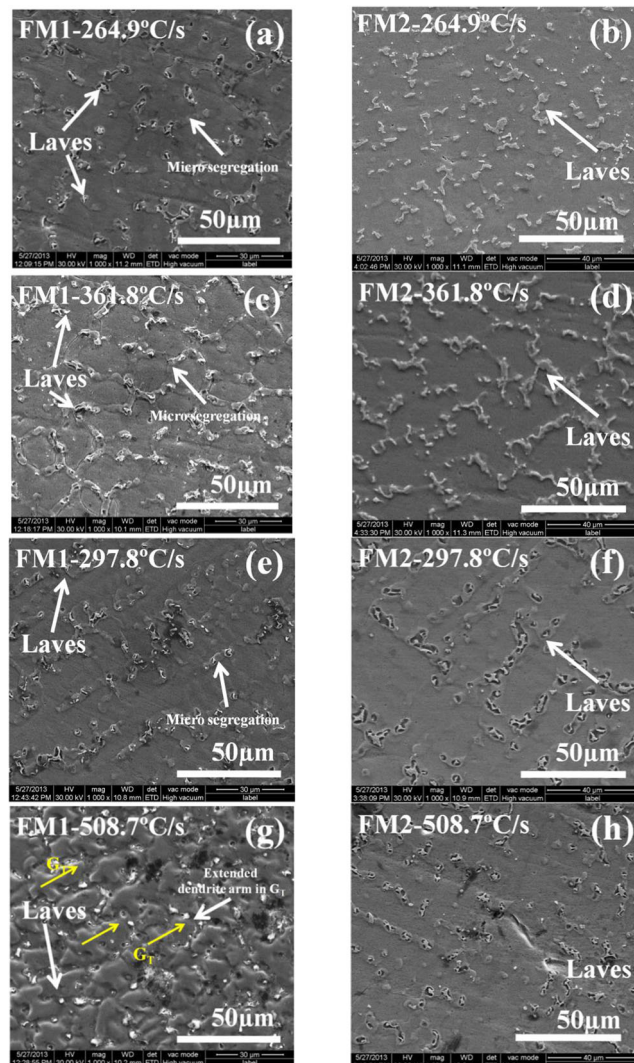


Fig. 4 SEM micrographs of the liquid nitrogen-cooled as-welded FM1 and FM2 fusion zones with an average weld cooling rate of **a, b** 264.9 °C/s, **c, d** 361.8 °C/s, **e, f** 297.8 °C/s, and **g, h** 508.7 °C/s

Fe content had a significant influence on the formation of eutectic. The reduction in dendrite Fe content of FM2 fusion zone (Table 3) for the increased average weld cooling rate resulted in minimizing the formation of Laves eutectic. FM1 fusion zone was having increased dendrite Fe content for the respective increase in average weld cooling rate. However, it was relatively lower than that of conventionally cooled fusion zone which aided in minimizing the Laves phase. The microstructures of the directly aged welded samples of FM1 (264.9 °C/s) and FM2 (264.9 and 361.8 °C/s) are shown in Fig. 5a, b, c. Comparing these microstructures with those in Fig. 4b, d (which were in as-welded condition), dissolution of the interdendritic phases occurred to a certain extent during the double aging process. This indicated that some metastable phases were getting dissolved during aging. The same has been further studied in X-ray diffraction analysis.

The interdendritic phases in the as-welded fusion zone of both the FM1 and FM2 fusion zones were found to be C14-type Laves phase with HCP crystal structure ($a=0.4831$ nm, $c=0.7881$ nm) as shown in Fig. 6a. The matrix was found to be face-centered cubic crystal structure ($a=0.3571$ nm) as in

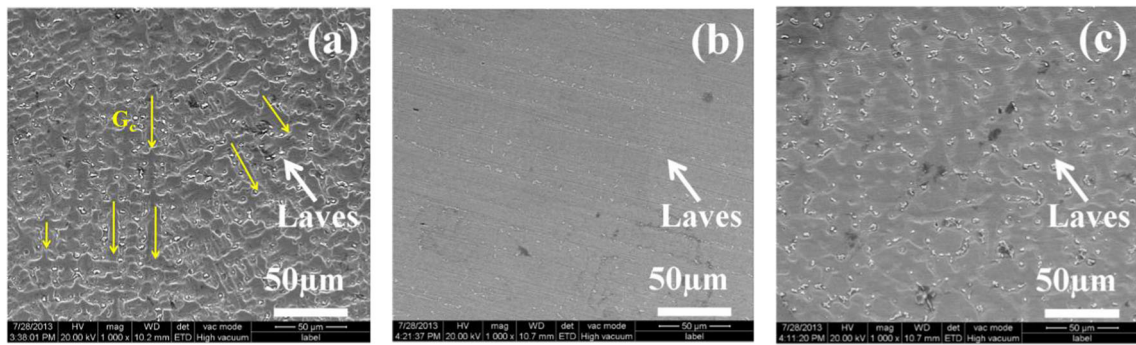


Fig. 5 Fusion zone in direct aged condition using **a** FM1 and **b, c** FM2

Fig. 6b. The crystal structure and the morphology of the laves phase did not change due to the imposed thermal gradient and enhanced weld cooling rate. The aging response was also confirmed by the TEM dark field images and the respective selected area diffraction patterns as shown in Fig. 6c, d. Disk-shaped γ'' precipitates and γ' precipitates were observed. The fundamental reflections were indicated for γ'' precipitates as shown in Fig. 6c. By the nature of solute elements present in the filler metal, FM2 fusion zone solidification ended up in a Laves eutectic reaction with “script” morphology as shown in Fig. 7a and FM1 fusion zone revealed an off-eutectic morphology as revealed in Fig. 7b.

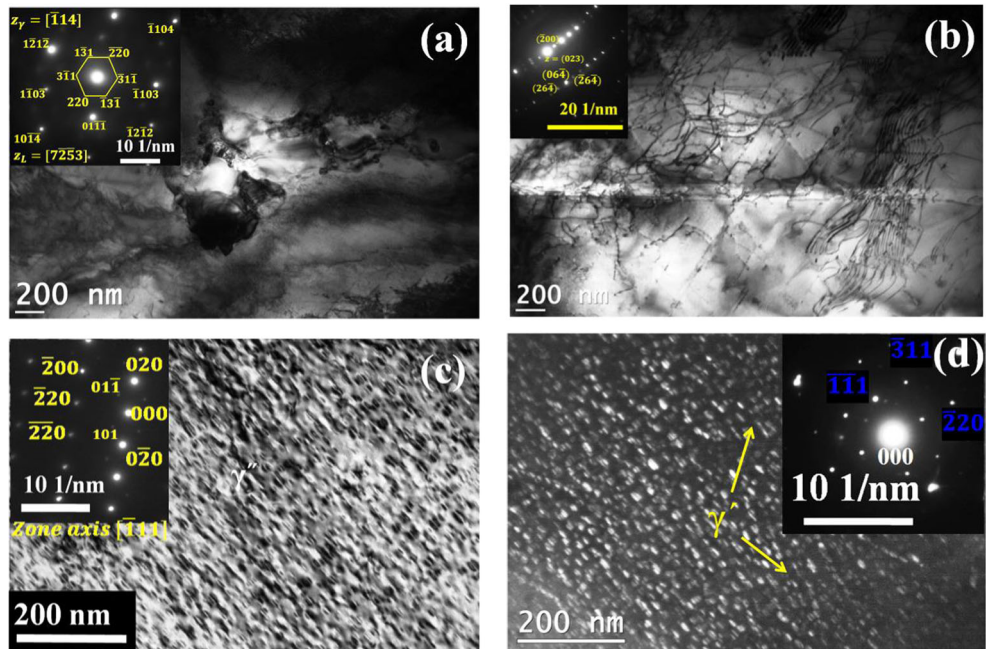
3.2 Microstructural characterization of heat-affected zone

The effect of heat input on heat-affected zone (HAZ) cracking in laser-welded ATI Allvac 718 superalloy was studied, and it was inferred that the steep temperature gradient and lower heat input led to HAZ liquation cracking (HAZ microfissuring)

[18, 19]. The heat-affected zone of welds made in the present work was found to be free from HAZ microfissuring as shown in Fig. 7c.

At the onset of welding process, the liquid nitrogen flow was maintained. The nucleate boiling heat transfer mechanism was operative in which large amount of heat flux was withdrawn at a lower temperature gradient. The cold nitrogen vapor generated during nucleate boiling was utilized for film boiling heat transfer in HAZ regime. The stresses during welding with LN₂ cooling could be higher due to the existence of a steep transverse temperature gradient in the welding direction. This thermal gradient effect was balanced by the cold nitrogen vapor with a temperature lower than the ambient temperature which was directed to HAZ through the side holes (row of holes of 6 mm diameter were made in the upper corner along the length of the copper fixture with an angle of attack in such a way that the liquid nitrogen vapor was directed toward the heat-affected zone as shown in Fig. 1c) in the copper fixture. This led to film boiling mode of heat transfer.

Fig. 6 TEM bright field images with SAD pattern of **a** laves phase and **b** matrix in as-welded fusion zone. TEM dark field images with SAD pattern of **c** γ'' precipitates and **d** γ' precipitate in direct aged fusion zone



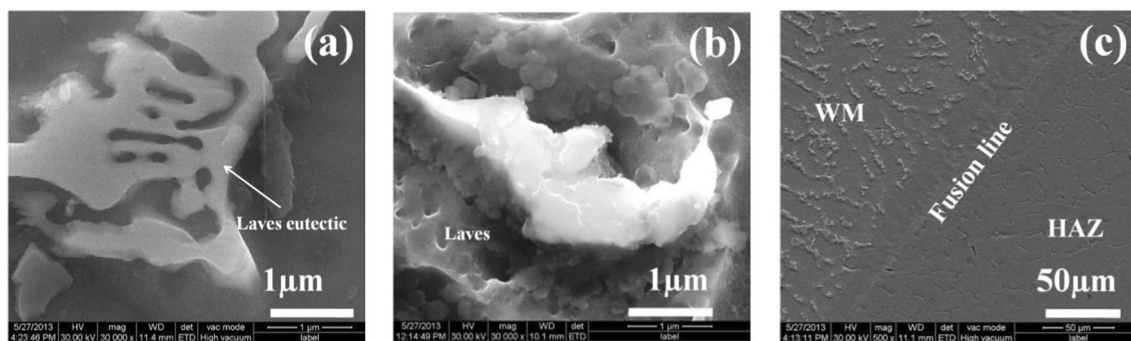


Fig. 7 SEM micrographs for the lave morphology in the fusion zone of **a** FM2 and **b** FM1 and **c** as-welded HAZ

Since the convective heat transfer was reduced, steep rise in temperature occurred. This avoided a steep transverse temperature gradient and thus the HAZ microfissuring. The investigations on HAZ of EB- and LB-welded alloy 718 were revealed with the microfissures [18, 19]. Since the high-energy-density welding processes were prone for microfissuring, using pulse GTA welding process with imposed external cooling resulted in a weld free of HAZ microfissures and reduced microsegregation.

3.3 Differential scanning calorimetric/thermal analysis of fusion zone

The fusion zone made using conventional cooling method was discussed in our previous work. The effects of weld cooling rate and weld metal chemistry on the characteristics temperature were studied [13]. The characteristic temperatures derived from the DSC and first derivative DTA thermograms of fusion zones with an average weld cooling rates of 264.9, 361.8, and 508.7 °C/s are given in Table 2. The characteristic temperatures measured during heating cycle of DSC and DTA experiments alone were discussed here because the elemental composition in the as-welded fusion zone had influence over the characteristic temperature during DSC/DTA heating cycle.

Since the DSC/DTA specimens were completely melted during heating and resolidified upon cooling, the influence of liquid nitrogen cooling on the microstructure was disturbed significantly during cooling cycle of DTA experiment. The liquidus temperature of FM1 fusion zone was differing from that of the FM2 fusion zone. Similar phenomenon was observed in the earlier works of Murata et al. (1994) due to the influence of microalloying elements, especially Mo content [20]. The trend of liquidus temperature of FM2 fusion zone decreased with the increased weld cooling rate from 264.9 to 508.7 °C/s as given in Table 2. This could be due to the reduced microsegregation as evidenced in the micrographs shown in Fig. 4b, d, h. Thus, more of solute contents (Nb and Mo) were retained in the matrix (Table 3), which substantiated the decreasing trend of the liquidus temperature [21–23]. The liquidus temperature for the fusion zone of an average weld cooling rate of 508.7 °C/s was comparable to the liquidus temperature of base material because of the reduced microsegregation.

The γ -NbC eutectic invariant temperature was in the range of 1220 to 1225 °C, and γ -lave eutectic invariant temperature was from 1180 to 1190 °C. Hence, it was inferred that the solidification sequence was not modified due to the rapid cooling. It was also observed that the eutectic reaction

Table 2 Details of characteristics temperature

Filler metal	Cooling rate (°C/s)	Reaction temperatures (°C) ±5 °C											
		Liquidus (T_L)				MC eutectic (T_{MC})			Lave eutectic (T_E)				
		DSC	DTA heating rate (°C/min)			DSC	DTA heating rate (°C/min)		DSC	DTA heating rate (°C/min)			
			20	10	5		20	10		5	20	10	5
FM1	264.9	1365	–	–	–	1220	–	–	1180	–	–		
	361.8	1369	–	–	–	1220	–	–	1180	–	–		
	508.7	1372	–	–	–	1220	–	–	1190	–	–		
FM2	264.9	1388	1395	1395	1394	1224	–	1220	1200	1189	–	–	1189
	361.8	1390	1390	1393	1385	1225	1220	1220	–	1190	1192	–	–
	508.7	1366	1363	1367	1365	1225	1206	1225	1250	1190	1180	1156	1188

Table 3 Elemental analysis of liquid nitrogen-cooled alloy 718 fusion zone using FE-SEM/EDS

Elements	Wt% of elements in dendrite							
	FM1				FM2			
	SD	264.9 °C/ s	361.8 °C/ s	508.7 °C/ s	SD	264.9 °C/ s	361.8 °C/ s	508.7 °C/ s
Al	±0.05	0.52	0.45	0.53	±0.06	0.67	0.54	0.55
Nb	±0.32	2.9	3.4	3.7	±0.65	2.6	3.2	3.3
Mo	±0.93	5	5	4.4	±1.64	5	5.4	6.7
Ti	±0.03	0.84	0.82	0.88	±0.18	1.12	0.75	0.77
Cr	±0.26	18	17.8	18.2	±0.37	18.4	17.8	17.6
Fe	±1.6	15.3	15	16.9	±3.25	19.8	14.5	13.4
Ni	±1.11	57.2	57.2	55.3	±4.19	52.3	57.8	57.5

temperatures were not modified for the same filler metal. The eutectic reaction temperatures were not affected by the cooling rate due to the complete melting and resolidification of the DSC/DTA specimen. However, the minor changes observed in the present study could be probably due to the variation in heating rates. Since the liquidus temperature was primarily influenced by the solute content, the same was reduced by the enhanced weld cooling rates for the same filler metal in the present work.

The FE-SEM/EDS analysis reported in the present work dealt with the composition of γ matrix. Because of the refined solidification structures obtained in the present work, there could be a difference in the compositions of the interdendritic precipitates and/or phases measured using FE-SEM/EDS analysis. Hence, those values were not reported here. However, the measured values of the elemental composition using FE-SEM/EDS were having better agreement with the previous works of Odabaşı et al. (2010) [24]. The presented data were pertaining to the elemental composition of the dendrite core. It was observed that the Mo concentrations in the as-welded fusion zones of both FM1 and FM2 filler metal were remaining same. This was due to the formation of Ni₄Mo phase in FM1 fusion zone in the as-welded condition. Similar phenomenon was observed in our earlier works [13, 25]. The existence of this phase reduced the Mo concentration in the dendrite core of FM1 fusion zone, and thus, the same was comparable with FM2 fusion zone even though the Mo content of FM1 filler metal was higher than that of FM2. The formation of the Ni₄Mo phase in the as-welded FM1 fusion zone was confirmed with X-ray diffraction and differential thermal analysis, and the same was discussed in detail in our previous work [25]. The formation of Ni₄Mo phase could probably be one of the reasons for the change in characteristic temperatures of the DSC/DTA curves.

The magnitude of microsegregation was assessed with the solidification parameters. The fineness of the microstructure was quantified with dendrite arm spacing measurement using

triangular method described elsewhere [13, 26]. Dendrite arm spacings were reduced from the range of 15–54 μm (conventional process) to 3–7 μm (LN₂-cooled process) for the employed process variables. The average weld cooling rate was calculated using Eq. (1) [6] and was found to be enhanced with LN₂ chilling than that of the conventional method.

$$\lambda_T = 518.39\varepsilon^{-0.592} \quad (1)$$

where λ_T is the dendrite arm spacing (μm) and ε is the weld cooling rate ($^{\circ}\text{C}/\text{s}$).

The variation of DAS with reference to the weld cooling rate was tabulated (Table 4). It was observed that the DAS was reduced with the enhanced weld cooling rate. Although this was an obvious phenomenon, the magnitude of DAS was significantly reduced, and thus, the microstructure of the fusion zone was significantly refined. The solidification time was calculated from the solidification range derived from the DSC analysis (Table 2) and the calculated weld cooling rate using Eq. (2). The local solidification time was drastically reduced with the enhanced weld cooling rate as shown in Table 4. This aided in reducing the microsegregation. The weld cooling rate was correlated to the solidification time as given in Eqs. (3) and (4). The volume fraction of the Laves phase was calculated using image analysis with the procedure mentioned in our previous work [13]. It was found that the Laves volume fraction was reduced from 35.7 to 3 vol% for FM1 fusion zone in the lower limits of the average cooling rate (43.2 and 264.9 $^{\circ}\text{C}/\text{s}$) as shown in Table 4. The Laves volume fraction of the FM2 fusion zone for the same range of weld cooling rate reduced from 45.95 to 1.2 vol%. A minimum 0.1 vol% of Laves phases was obtained in the fusion zone with the average weld cooling rate of 508.7 $^{\circ}\text{C}/\text{s}$. Similarly, Laves particle size was measured to be in the range of 1.43 to 0.04 μm as given in Table 4. The size of laves

Table 4 Details of SR and lave volume fraction

Weld cooling rate (°C/s)	Filler metal	DAS (μm)	Segregation ratio		Average lave volume fraction (%)	Lave particle size (μm)	Microsegregation index		$\Delta T = T_L - T_E$ (°C)	t_s (s)
			SR _{Nb}	SR _{Mo}			Nb	Mo		
264.9	FM1	19.06	6.8	0.83	3	1.434	0.9518	0.9995	185	0.69
	FM2	20.02	7.8	0.75	1.2	0.376	0.9562	0.9996	199	0.75
361.8	FM1	18.86	5.9	0.83	0.7	0.427	0.9508	0.9995	189	0.52
	FM2	19.81	6.4	0.75	0.1	0.09	0.9553	0.9996	200	0.55
508.7	FM1	10.35	4.4	0.95	0.4	0.224	0.8456	0.9984	182	0.36
	FM2	10.17	4.1	0.7	0.1	0.04	0.8406	0.9984	176	0.35

particle was calculated from the average values of at least 15 sets of FE-SEM micrographs.

$$t_s = \frac{\Delta T}{\varepsilon'} \quad (2)$$

$$t_s^{\text{FM1}} = 14.446\varepsilon'^{-0.812}, R^2 = 0.99 \quad (3)$$

$$t_s^{\text{FM2}} = 13.83\varepsilon'^{-0.781}, R^2 = 0.88 \quad (4)$$

where s is the solidification time, FM1 is the solid solution filler metal, FM2 is the age-hardenable filler metal, ε' is the cooling rate (°C/s), and ΔT is the solidification temperature range (°C).

The interdendritic segregation was represented by the residual microsegregation index model [27] developed by Flemings (1974) as in Table 4. This index was useful in predicting the homogenization temperature and/or time. The diffusivity of Nb in γ -Fe was considered, since the formation of Fe_2Nb was confirmed in the electron and X-ray diffraction analysis. Following parameters were used for the calculation of solute diffusivity [28, 29]:

$$\begin{aligned} D_0^{\text{Nb}} &= 7.5 \times 10^{-5} \text{m}^2/\text{s}, \text{ Activation energy } Q \\ &= 264 \text{ kJ/mol}, D_s^{\text{Ni-Mo}} \\ &= 1.5 \times 10^{-19} \text{m}^2/\text{s at } 800^\circ\text{C} \end{aligned}$$

The diffusivity of Nb in γ -Fe was calculated for the temperature of 720 °C (first step temperature in two-step aging heat treatment for 8 h). The variation of MSI (δ) on the average weld cooling rate was analyzed. The microsegregation index values for both Nb and Mo were calculated. The microsegregation index of Nb (δ -Nb) was slightly reduced with increased weld cooling rate which indicated a reduction in microsegregation.

The δ -Nb of fusion zone cooled with liquid nitrogen was approaching 0.85. The highest computed cooling rate of 508.7 °C/s produced fusion zone with the lowest volume fraction of Laves phase as shown in Fig. 4g, h. The microsegregation of Mo was approaching to unity in all the cases, which indicated that the Mo segregation was insensitive to cooling rate. The values of δ for both Nb and Mo in the conventionally cooled fusion zone exhibited unity. Thus, the conventional method could not effectively reduce the formation of laves phases. It was inferred from the microsegregation index that the homogenization of liquid nitrogen-cooled fusion zone would be requiring a minimum time at 1140 °C. The volume fraction of Laves phase was calculated using image analysis with FE-SEM images taken at regular intervals in the fusion zone. The segregation ratio (SR) was calculated in the as-welded condition of the each fusion zone. The details of the SR and volume fraction are as given in Table 4.

Substantial variation in segregation ratio between FM1 and FM2 was not observed at a higher weld cooling rate, since the solidification time was lower at higher weld cooling rates. The elemental segregation was defined by the equilibrium partition ratio calculated using Brody and Flemings model [27]. The back diffusion constant α was calculated using Flemings model [27] for each average weld cooling rate with the parameters such as ΔT from Table 4, $D_0 = 7.5 \times 10^{-5} \text{m}^2/\text{s}$ for the diffusion of Nb in γ -Fe matrix [28], $Q = 264 \text{ kJ/mol}$. The measured liquidus and eutectic temperatures, solidification time, and dendrite arm spacing values were used to compute the back diffusion constant. It yielded values of α for Nb (0.002 to 0.005) immensely less than 1. The same was compared using Clyne-Kurz model, and it was equal to the Flemings model since $\alpha \ll 1$.

The values for α_{Nb} were marginally increased for the liquid nitrogen-cooled fusion zone than that of the conventionally cooled fusion zones. However, these values were very much less than 1 and the diffusion of Nb in solid was neglected

Table 5 Details of partition coefficient of alloying elements at the start of solidification

Cooling rate (°C/s)	Partition coefficient											
	Al		Nb		Mo		Ti		Cr		Fe	
	FM1	FM2	FM1	FM2	FM1	FM2	FM1	FM2	FM1	FM2	FM1	FM2
264.9	0.8	1.1	0.6	0.4	1.7	1	0.8	1.1	0.99	1	0.8	1
361.8	0.7	0.9	0.7	0.6	1.7	1.9	0.8	0.8	0.98	0.98	0.8	0.7
508.7	0.9	0.9	0.7	0.6	1.5	2.3	0.9	0.8	1	0.97	0.9	0.7

under the employed solidifying conditions. Hence, the partition ratio was calculated at the onset of solidification using the ratio between elemental concentration at dendrite core and nominal concentration. The details are tabulated in Table 5. The partitioning ratio of Fe in FM1 and FM2 fusion zones exhibited more of Fe partitioning toward dendrite which resulted in Nb partitioning toward interdendrite as the solubility of Nb was proved to be reduced with enhanced Fe content. The partitioning ratio of Cr was approaching unity for all the experimental cases. Hence, γ matrix was enriched with Cr. The base material was having 18.15 wt% Cr and filler metals FM1 and FM2 were containing 16 and 21 wt% Cr, respectively.

An average Cr content of 18 wt% was observed in the dendrite core as in Table 3. As the average cooling rate was increased from 264.9 to 508.7 °C/s, the Fe content (19.8 to 13.4 wt%) in γ matrix of FM2 fusion zone and k_{Fe} were reduced, which aided in solubility of Nb and Mo in dendrite, and thus, the interdendritic segregation was also reduced. The solubility limit of solute elements (Nb, Mo) was varying with respect to the solvent/matrix elements (Ni, Fe, Cr) and the temperature. In order to predict the nature of the interdendritic phase, the partition ratio of solute elements was calculated for each of the matrix element at its maximum limit of solid solubility.

The partition ratio at the terminal stage of solidification was calculated with reference to the matrix element for two of the employed average weld cooling rates (264.9 and 508.7 °C/s) of FM2 fusion zone in the present study. The EPMA data

(Table 6) were used for the calculation of partition ratio. The maximum solubility of the solutes (Nb and Mo) in the solvents (Ni, Fe, and Cr) was divided by the respective elemental concentration in the eutectic constituent [30]. The interdendritic regions were assumed as liquid, since those regions were terminally solidified. The details are given in Table 7.

It was observed that the partitioning ratio of Nb in Ni was increased with enhanced weld cooling rates. Moreover, the partitioning ratio of Nb in Ni matrix at the terminal stage solidification was approaching 0.5. Thus, the formation of Ni_2Nb partially existed. The k_{Nb} in Fe matrix was very much lower and approaching zero. Hence, the segregation of Nb in Fe matrix occurred. This led to the formation of Fe_2Nb . Moreover, the k_{Nb} in Cr matrix was in the range of 0.49 to 0.50. Since the partitioning ratio of Nb in Fe matrix was very much lower, the possibility for the formation Fe_2Nb existed.

The solidification parameters such as SR, microsegregation index (MSI), and partition ration (k) were correlated with the weld cooling rates for the solute contents Nb and Mo. The details of the same are given in Fig. 8a, b. The segregation ratio of Nb was decreasing with the increased cooling rate, and similarly, the partitioning behavior of the element was approaching toward dendrites ($k=0.74$). A minor reduction in microsegregation index of Nb was also substantiating the obtained results. But, the segregation and partitioning behavior of Mo was not following the explained phenomenon. Hence, it could be inferred that the segregation and partitioning behavior of Mo was insensitive to cooling rate.

Table 6 Quantitative analysis of alloy 718 fusion zone in EPMA

Process	Zone	Elements (wt%)							
		Ti	Ni	Fe	Cr	Mo	Nb	Si	Al
CCP-conventional cooling (394.3 °C/s)	DC	0.46±0.04	58.55±0.32	14.19±0.37	17.16±0.12	5.58±0.12	1.69±0.08	0.05±0.01	0.38±0.01
	Laves	0.99±0.23	42.44±3.48	8.56±0.29	13.02±0.09	11.87±0.25	20.59±0.6	0.35±0.08	0.19±0.02
CC-LN ₂ cooling (264.9 °C/s)	DC	0.62±0.003	52.52±0.17	21.47±0.17	18.75±0.11	2.28±0.10	1.88±0.16	0.05±0.01	0.52±0.04
	Laves	1.79±0.05	45.3±1.14	13.19±0.17	13.32±0.26	3.93±0.12	20.04±0.12	0.39±0.03	0.35±0.02
CCP-LN ₂ cooling (508.7 °C/s)	DC	0.68±0.12	52.41±0.50	20.51±0.48	18.45±0.23	2.41±0.13	2.19±0.45	0.06±0.03	0.57±0.02
	Laves	1.69±0.02	43.77±1.21	13.39±0.46	13.3±0.14	4.14±0.08	20.11±0.04	0.35±0.06	0.35±0.05

DC dendrite core

Table 7 Partition ratio at the terminal stage of solidification

Solvent (matrix)	Solute	Maximum solid solubility (wt%)	<i>k</i> at the terminal stage of solidification	
			264.9 °C/s	508.7 °C/s
Ni	Nb	9.3	0.47	0.47
	Mo	16	4.07	3.86
Fe	Nb	1.5	0.075	0.075
	Mo	2.9	0.74	0.70
Cr	Nb	10	0.50	0.50
	Mo	100	25.45	24.15

3.4 X-ray diffraction analysis

Bright interdendritic phases were observed in the fusion zone during electron microscopic study. These phases were identified as Laves phases and/or MC-type carbides in the previous studies of alloy 718 weldments [31]. The microstructural parameters of coherent precipitates in Inconel 625 were studied using an X-ray diffraction technique on the bulk samples [32]. Hence, similar procedure was adopted for the present work. The diffraction peaks for Laves phase were found to be weaker and observed at lower weld cooling rates. In addition, Ni₄Mo peaks were observed in the as-welded FM1 fusion zone. These peaks were comparable to those in the earlier studies on the crystal structure of Ni₄Mo. The tetragonal distortion of cubic close-packed structure occurred due to the ordering reaction at 840 °C after quenching from above 900 °C in Ni-20 at% Mo [33]. Such transformation could have occurred upon solidification and led to the formation of Ni₄Mo in the present study.

The γ'' peaks were observed after aging of the welded samples as in Table 8. The reference diffraction peaks for γ'' precipitates were derived from the previous work on alloy 718 [34]. Since the γ'' diffraction peaks could match with the diffraction peaks of δ phase, the

existence of γ'' precipitates was confirmed by TEM analysis as in Fig. 6c. During direct aging treatment, γ'' phase was nucleated from Laves phase as revealed in diffraction patterns. This confirmed the aging response of the FM1 fusion zone. Details of the diffraction peaks are as listed in Table 8.

The imposed temperature gradient using liquid nitrogen during solidification led to a reduced solidification time. This helped in reducing the microsegregation. Upon solidification, the Nb was utilized for the formation of NbC, and hence, the Nb became unavailable for the formation of Laves phase. The diffraction peaks corresponding to Laves phase were not observed in the liquid nitrogen-cooled fusion zone with an average weld cooling rate of 508.7 °C/s. Hence, it could be inferred that the volume fraction of Laves phase was less than 5 %. The diffraction peak of β phase was sharp in lower weld cooling rate (264.9 °C/s). The possibility of forming metastable Ni₂Mo phase was reported during quenching from γ -solid solution for the lowest concentration of Mo in solution [35]. The ordering and the effect of ternary elements on the stability of ordered phases in Ni-Mo binary systems and Ni-Al-Mo ternary system were studied and confirmed the existence of metastable Ni₄Mo and Ni₂Mo phases [35–38]. The Ni solid solution was present up to 16 wt% Mo, and Ni₄Mo existed at 29 wt% Mo in Ni-Mo binary system [39]. Hence, Ni₄Mo could be present with Ni between 16 and

Fig. 8 Correlation of solidification parameters with weld cooling rate for e Nb and f Mo

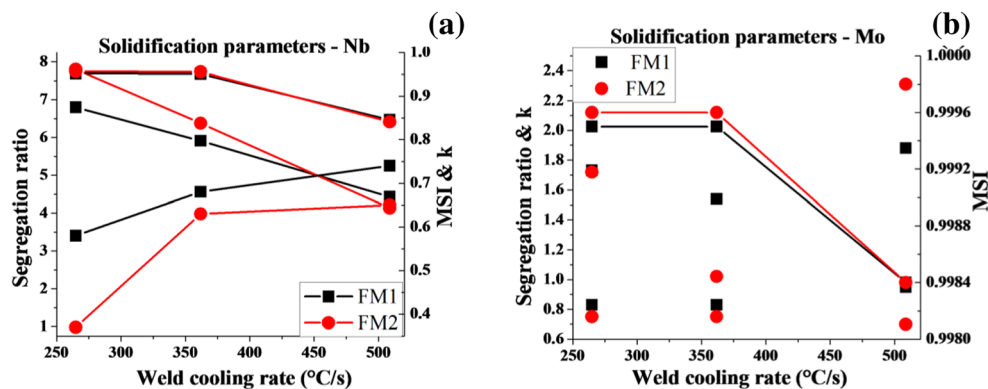


Table 8 Details of X-ray diffraction peaks

Phase	2θ			hkl	Lattice details	PDF Ref
	264.9 °C/s	361.8 °C/s	508.7 °C/s			
As-welded condition-FM1						
γ (Ni _{2.4} Cr _{0.7} Fe _{0.36})	43.59	43.64	43.52	111	FCC, 0.3553 nm $Fm\bar{3}m$	330945
	50.7	50.72	50.66	200		
	74.53	75.59	74.69	220		
	90.33	92.22	91.37	311		
	97.23	97.79	96.86	222		
Laves (Fe ₂ Nb)	24.36	24.09	–	101	HCP, P6 ₃ /mmc, $a=0.4831$ nm, $c=0.7881$ nm	653574
	37.42	37.23	–	110		
	43.59	–	–	112		
	56.03	56.13	–	203		
β (Ni ₄ Mo)	30.9	31.4	31.29	200	BCT, I4/m, $a=0.572$ nm, $c=0.3564$ nm	655480
	43.59	–	43.79	121		
	50.9	50.9	50.66	310		
	74.53	74.58	–	312		
MC [Nb(C,N)]	34.88	34.73	34.79	111	FCC, 0.4469 nm $Fm\bar{3}m$	893890
	40.39	–	40.35	200		
	58.21	58.72	57.76	220		
	69.26	69.75	69.58	311		
As-welded condition-FM2						
γ (Ni _{2.4} Cr _{0.7} Fe _{0.36})	43.78	43.83	43.62	111	FCC, 0.3553 nm $Fm\bar{3}m$	330945
	51.07	51.01	50.75	200		
	75.76	75.31	75.19	220		
	90.25	92.25	92.33	311		
	96.02	97.23	–	222		
Laves (Fe ₂ Nb)	37.09	–	–	110	HCP, P6 ₃ /mmc, $a=0.4831$ nm, $c=0.7881$ nm	653574
	43.09	43.11	–	112		
	50.65	–	–	104		
	62.98	62.98	–	105		
MC [Nb(C,N)]	35.04	34.57	34.88	111	FCC, 0.4469 nm $Pm\bar{3}m$	893890
	40.13	40.5518	40.83	200		
	58.35	–	–	220		
	–	69.39	69.73	311		
Direct aged condition-FM1						
γ'' (Ni ₃ Nb)	35.58	36.02	36.64	110	BCT, $a=0.3624$ nm, $c=0.7406$ nm, I4/m	[34]
	42.85	–	–	112		
	49.13	49.72	49.06	004		
	73.43	73.7	73.19	204		
	89.54	–	–	312		
	93.84	–	–	224		
γ' (Ni ₃ Al)	35.58	–	–	110	FCC, 3.571 nm $Pm\bar{3}m$	656613
	43.68	42.19	41.81	111		
	50.84	49.59	49.06	200		
	74.66	74.21	73.19	220		
	90.69	–	–	311		
	96.48	–	–	222		
Laves (Fe ₂ Nb)	31.55	–	–	102	HCP, P6 ₃ /mmc, $a=0.4831$ nm, $c=0.7881$ nm	653574
	37.19	51.2	–	110		
	51.2	–	–	104		
	75.22	–	–	220		

Table 8 (continued)

Phase	2θ			hkl	Lattice details	PDF Ref
	264.9 °C/s	361.8 °C/s	508.7 °C/s			
MC [Nb(C,N)]	35.58	35	–	111	FCC, 0.4469 nm $Pm\bar{3}m$	893890
	–	40.55	–	200		
	–	–	–	220		
	–	–	–	311		
	73.36	–	–	222		
Direct aged condition-FM2						
γ'' (Ni ₃ Nb)	35.05	–	35.89	110	BCT, $a=0.3624$ nm, $c=0.7406$ nm, I4/m	[34]
	–	–	–	112		
	–	49.00	48.52	004		
	–	–	–	200		
	–	72.18	72.22	204		
γ' (Ni ₃ Al)	35.58	35.54	35.89	110	FCC, 3.571 nm $Pm\bar{3}m$	656613
	43.68	43.67	43.95	111		
	50.95	50.86	51.01	200		
	74.88	74.82	75.07	220		
Laves (Fe ₂ Nb)	35.05	–	–	102	HCP, P6 ₃ /mmc, $a=0.4831$ nm, $c=0.7881$ nm	653574
	–	–	35.89	110		
	42.59	40.57	–	103		
	–	43.67	–	112		
	50.95	–	–	104		
MC [Nb(C,N)]	35.05	–	35.89	111	FCC, 0.4469 nm $Pm\bar{3}m$	893890
	40.89	40.57	40.96	200		
	59.60	–	57.45	220		
	–	–	–	222		

29 wt% of Mo in Ni-Mo binary system. These metastable phases were dissolved to a certain extent during aging treatment [25] to a certain extent and resulted in the microstructures shown in Fig. 6a, b, c.

In order to study the influence of the increased solute content (Mo) in the matrix on the lattice parameter, those values were calculated by Nelson-Riley method and reported in Table 9. The lattice parameter of γ matrix was computed from the X-ray diffraction data using Nelson-Riley extrapolation functions. The weld cooling rate also had an influence on the lattice parameter. The lattice parameter of the gamma matrix was increased with enhanced weld cooling rate due to the availability of solute in the matrix. The results of the lattice

parameter computation in the present work were comparable with the previous investigations in Ni-Mo binary system. The lattice parameters (0.35238 to 0.35917 nm for Mo, 0 to 17 at%/0 to 25.08 wt%) were measured for the different composition of Mo in Ni-Mo binary system. The lattice parameters of both the fusion zones are given in Table 9.

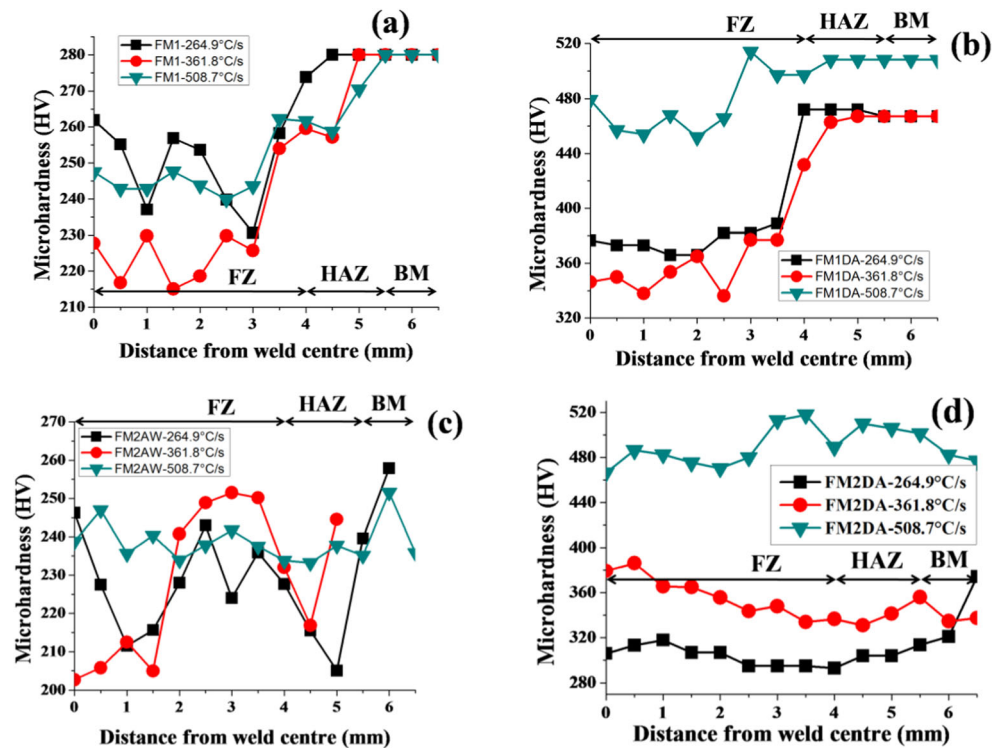
$$\left. \begin{aligned} a_{\gamma}^{FM1} &= 0.35349 + 2.89407 E^{-6} \varepsilon \\ a_{\gamma}^{FM2} &= 0.35653 + 1.07025 E^{-7} \varepsilon \end{aligned} \right\} \quad (15)$$

where a_{γ}^{FM1} is the lattice parameter of γ matrix in FM1 fusion zone, a_{γ}^{FM2} is the lattice parameter of γ matrix in FM2 fusion zone, and ε is the weld cooling rate (°C/s).

Table 9 Details of lattice parameter computed from XRD data

Weld cooling rate (°C/s)	Lattice parameter of γ matrix (nm)			
	Nelson-Riley method			
	FM1	Mean	FM2	Mean
264.9	0.355933	0.35799 ± 0.00545	0.357772	0.3567 ± 0.00098
361.8	0.3552		0.356568	
508.7	0.366131		0.357018	

Fig. 9 Microhardness survey of weldment made using **a** FM1, **c** FM2 in as-welded condition and **b** FM1, **d** FM2 in direct aged condition



3.5 Microhardness measurement

The microsegregation and aging response were assessed by microhardness survey across the weld zone. Figure 9a, b shows the microhardness measurement of the FM1 fusion zone in as-welded and direct aged conditions, respectively. The reported values were the average of five measurements at each point, and a scatter of $\pm 5\text{--}8\%$ was observed. The hardness in the as-welded condition for the four different cooling rates was in the range of 225 to 275 HV, whereas the same for the FM2 fusion zone was in the range of 200 to 250 HV as shown in Fig. 9c. The higher hardness in the as-welded condition in the case of FM1 could be due to the interdendritic phases in the FM1 fusion zone as in Fig. 4a, c, g.

In addition, the retained solute element (Mo) in matrix promoted solid solution strengthening, which also aided in enhancing the hardness of the fusion zone. The microhardness measurements of FM1 fusion zone revealed the aging response of the fusion zone. The hardness of the FM1 fusion zone after aging was comparable with the FM2 fusion zone for the same cooling rate of 508.7 °C/s as shown in Fig. 9b, d. The transition of hardness from fusion zone to base material was smoother in the 508.7 °C/s FM1 fusion zone. In the case of the FM1 fusion zone with the average weld cooling rates of 264.9 and 361.8 °C/s, steep transition of hardness was observed after direct aging. This could be because of the depletion of strengthening element (Nb) in the fusion zone. The maximum hardness value obtained for the conventionally welded samples of FM1 was 420 Hv and 450 Hv for FM2. The hardness value was increased to 475 Hv when LN₂ cooling was employed

for both the fusion zones of FM1 and FM2. The FM1 fusion zone was responded for aging comparable to the FM2 fusion zone at higher cooling rate, since the microsegregation was considerably controlled. This minimized the depletion of the useful strengthening element (Nb) as evidenced in Table 3.

4 Conclusion

The present work investigated the Nb segregation and Laves phase formation in alloy 718 fusion zone upon solidification. This is a persistent problem in many aerospace industries even after decades of alloy 718 invention. The formation of Laves phase during welding in the aerospace components affected the performance of those systems. Especially in the rocket propulsion, this has a greater impact on the mission. The current problem of Laves phase formation has been approached with enhancement of weld cooling rate. From the investigations carried out on Laves phase formation in alloy 718 fusion zone, the following conclusions are arrived at:

- The microsegregation was reduced when cryogenic cooling was employed during GTA welding process. The microstructures have been refined by the acceleration of morphology parameter (G/R) and GR due to the higher thermal gradients. The solidification rates were found to be increased in compound current pulse process with helium shielding gas and liquid nitrogen cooling. The negative longitudinal temperature gradient promoted while

using helium shielding gas enhanced the weld cooling rate. This enhanced cooling rate was useful in order to minimize cycle time and to refine microstructures.

- The weld cooling rates were derived from the dendrite arm spacing. The laves volume fraction was reduced to a minimum as 0.1 % at a weld cooling rate of 508.7 °C/s. The maximum laves volume fraction in liquid nitrogen-cooled GTAW process was 3 % at a weld cooling rate of 264.9 °C/s, which was lower than the conventional cooled GTAW process by 50 %. The fusion zone microstructures were refined with a dendrite arm spacing of 10–20 μm.
- It has been inferred from the experimental results that enhanced weld cooling rate reduced the interdendritic segregation and thereby improved the response for aging treatment. The fusion zone hardness after direct aging was obtained as 475 Hv in both FM1 and FM2 fusion zones.
- The novel idea of using liquid nitrogen for the external cooling upon solidification has been studied with a precaution to eliminate ice formation in order to avoid porosities in the fusion zone. The beneficial effect of liquid nitrogen cooling upon solidification of alloy 718 fusion zone is demonstrated. In this method, the cooling rate has been drastically enhanced by increasing the longitudinal temperature gradient along weld
- The microsegregation of Nb followed a downward trend with enhanced cooling rates. This was quantified with the segregation ratio of Nb. A reduction in segregation ratio of Nb was observed from 6.38 to 4.13. But for Mo, the phenomenon is not a function of cooling rate.
- The present attempt of enhancing the cooling rate with liquid nitrogen is better approach in laboratory level for studying the effects of high solidification and cooling rates. However, the limitations for practical implementation need to be further investigated.

References

1. Böttger B, Grafe U, and MaD, (2000) Prediction and measurement of microsegregation and microstructural evolution in directionally solidified superalloys. In: Pollock CM, Kissinger RD, Bowman RR, Green KA, McLean M, Olson S, Schirra JJ (Eds.) Proceedings of Superalloys 2000, The Minerals, Metals & Materials Society, 2000, 313–322.
2. Radhakrishna C, Prasad Rao K, Srinivas S (1995) Laves phase in superalloy 718 weld metals. *J Mater Sci Lett* 14:1810–1812
3. Janaki Ram GD, Prasad RK, Madhusudhan Reddy G (2004) Control of Laves phase in Inconel 718 GTA welds with current pulsing. *Sci Technol Weld Join* 5(9):390–398
4. Janaki Ram GD, Venugopal Reddy A, Madhusudhan Reddy G, Prasad Rao K (2005) Improvement in stress rupture properties of Inconel 718 gas tungsten arc welds using current pulsing. *J Mater Sci* 40:1497–1500
5. Manikandan SGK, Sivakumar D, Prasad Rao K, Kamaraj M (2012) Control of Laves phase in Inconel 718 weldments. *Mater Sci Forum* 710:614–619
6. Manikandan SGK, Sivakumar D, Prasad Rao K, Kamaraj M (2014) Effect of weld cooling rate on Laves formation in Inconel 718 fusion zone. *J Mater Process Technol* 214(2):358–364. doi:10.1016/j.jmatprotec.2013.09.006
7. Manikandan SGK, Sivakumar D, Karthikesan D, Prasad Rao K, Kamaraj M (2013) Frequency modulation effect on the solidification of alloy 718 fusion zone. *Process Mater Sci Technol* 1:1375–1361
8. Madhusudhana Reddy G, Srinivasa Murthy CV, Srinivasa Rao K, Prasad Rao K (2009) Improvement of mechanical properties of Inconel 718 electron beam welds—influence of welding techniques and post weld heat treatment. *Int J Adv Manuf Technol* 43:671–680
9. Amuda MOH, Mridha S (2013) Grain refinement and hardness distribution in cryogenically cooled ferritic stainless steel welds. *Mater Des* 47:365–371. doi:10.1016/j.matdes.2012.12.008
10. Gabzdyl J (2002) Cryogenic weld cooling. *Ind Laser Solut* 17(5): 25–29
11. Needham JC (1972) Joining of metals by the pulsed TIG process—a solution to manage welding problems. *Aus Weld J* 16(5).
12. Boughton P (1971) High precision pulsed TIG welding. Paper no-10. Proc. Conf. on Adv. Welding Processes. Weld. Intl.
13. Manikandan SGK, Sivakumar D, Prasad Rao K, Kamaraj M (2015) Laves phase in alloy 718 fusion zone—microscopic and calorimetric studies. *Mater Charact* 100:192–206
14. Lee HT, Jeng SL, Kuo TY (2003) The microstructure and fracture behavior of dissimilar alloy 690-SUS304L joint with various Nb addition. *Metall Mater Trans A* 34A:1097–1105
15. Jeng SL, Lee HT, Kuo TY, Chung CL, Huang JY (2015) The effects of Mn and Nb on the microstructure and mechanical properties of alloy 152 welds. *Mater Des* 87:920–931
16. Kuo TY, Lee HT, Tu CC (2003) An evaluation of the effects of Nb and Mn addition on the nickel base weldments. *Sci Technol Weld Join* 8(1):39–48
17. Brandao WJ, Bueno VTL, Marques PV, Modenesi PJ (1992) Avoiding problems when welding AISI 430 ferritic stainless steel. *Weld Int* 6:713–716
18. Idowu OA, Ojo OA, Chaturvedi MC (2007) Effect of heat input on heat affected zone cracking in laser welded ATI Allvac 718Plus superalloy. *Mater Sci Engg* 454–455(25):389–397
19. Vishwakarma KR, Richards NL, Chaturvedi MC (2008) Microstructural analysis of fusion and heat affected zones in electron beam welded ALLVAC® 718PLUS™ superalloy. *Mater Sci Engg A* 480(1–2):517–528
20. Murata Y, Morinaga M, Yukawa N, Ogawa H and Kato M. (1994) Solidification structures of Inconel 718 with microalloying elements, In: E.A. Loria (Ed.) Superalloys 718,625,706 and Various Derivatives, The Minerals, Metals & Materials Society, 81–88.
21. Cieslak MJ, Headley TJ, Knorovsky GA, Romig AD Jr, Kollie T (1990) A comparison of the solidification of Incoloy 909 and Inconel 718. *Metall Trans* 21A:479–488
22. Beckers JL (1988) Study of solidification features of nickel base superalloys in relation with composition. *Metall Trans A* 19:2333–2340
23. Fusner E (2013) Elemental effects of Fe, Mo, C and Hf (or Nb) on solidification behavior, microstructure and weldability of high Cr nickel base filler metals. MS dissertation, Ohio State University.
24. Odabaşı A, Ünlü N, Göller G, Eruslu MN (2010) A study on laser beam welding (LBW) technique: effect of heat input on the microstructural evolution of superalloy Inconel 718. *Metall Mater Trans A* 41A:2357–2365
25. Manikandan SGK, Sivakumar D, Kamaraj M (2015) Phase transformation studies in alloy 718 fusion zone welded using high Mo

- filler metal. Symposium in the recent trends in the plasticity and phase transformations. Ruhr University, Bochum
26. Rocha OL, Siqueira CA, Garcia A (2003) Heat flow parameters affecting dendrite spacings during unsteady state solidification of Sn–Pb and Al–Cu alloys. *Metall Mater Trans A* 34(4):995–1006
 27. Flemings MC (1974) *Solidification processing*. Mc-Graw Hill Inc., Ch. 10, 330.
 28. Kurokawa S, Ruzzante E, Hey AM, Dyment F (1983) Diffusion of Nb in Fe and Fe alloys. *Metal Sci* 17:433–438
 29. Chou TC, Nieh TG (1991) Explosive anisotropic grain growth of δ -NiMo by solid state diffusion. *Appl Phys Lett* 58(23):2642
 30. Knorovsky GA, Cieslak MJ, Headley TJ, Romig AD Jr, Hammett WF (1989) Inconel 718: a solidification diagram. *Metall Mater Trans A* 20(10):2149–2158
 31. Sivaprasad K, Ganesh Sundararaman S (2008) Influence of weld cooling rate on microstructure and mechanical properties of alloy 718 weldments. *Metall Mater Trans A* 39(9):2115–2127
 32. Mukherjee P, Sarkar A, Barat A, Jayakumar T, Mahadevan S, Sanjay RK (2008) Lattice misfit measurement in Inconel 625 by X-ray diffraction technique. *Int J Mod Phys B* 22(23):3977–3985. doi:10.1142/S0217979208048772
 33. Harker D (1944) The crystal structure of Ni₄Mo. *J Chem Phys* 12(7): 315–317
 34. Choi HS, Choi J (1972) Precipitation in Inconel 718 alloy. *J Korean Nucl Soc* 4(3):203–213
 35. Saburi T, Komatsu K, Yamamoto M, Nenno S, Mizutani Y (1969) A new metastable phase Ni₂Mo. *Trans AIME* 245:2348–2349
 36. Arya A, Banerjee S, Das GP, Dasgupta I, Saha-Dasgupta, Mookerjee A (2001) A first principle thermodynamics approach to ordering in Ni-Mo alloys. *Acta Mater* 49:3575–3587
 37. Arya A, Kulkarni UD, Dey GK, Banerjee (2008) Effect of ternary additions on the stability of ordered phases in Ni-Mo alloys—transmission electron microscopy results and first principles calculation. *Metall Mater Trans A* 39A:1623–1629
 38. Kersker MM (1986) *Precipitation in nickel-aluminum-molybdenum superalloys*. University of Florida. <http://ufdc.ufl.edu/UF00085802/00001>
 39. Okamoto H (1991) Molybdenum-nickel. *J Phase Equilib* 12(6):703